JOURNAL OF AIRCRAFT
Vol. 39, No. 3, May–June 2002

Optimal Dynamic Response Control of Elastically Tailored Nonuniform Thin-Walled Adaptive Beams

Sungsoo Na*
Korea University, Seoul 136-701, Republic of Korea
and
Liviu Librescu†
Virginia Polytechnic Institute and State University, Blacksburg, Virginia 24061-0219

A dual approach based on structural tailoring and adaptive materials technology aimed at controlling the dynamic response of tapered thin-walled beams exposed to external pressure pulses is presented. Whereas structural tailoring uses the directionality properties of advanced composite materials, the adaptive materials technology exploits the actuating and sensing capabilities of piezoelectric material systems bonded or embedded into the host structure. The structure is modeled as a doubly tapered composite thin-walled beam incorporating a number of nonclassical features such as transverse shear, warping inhibition, anisotropy of constituent materials, and rotatory inertias. The cases of piezoactuators spread over the entire span of the structure or in the form of a patch are considered, and issues related to the influence of patch location and size on the control efficiency are discussed. Other issues related to the implications of the inclusion/discard in the quadratic performance index of time-dependent external excitations are also addressed. The displayed numerical results provide a comprehensive picture of the synergistic implications of the application of both techniques, namely, the tailoring and optimal control on vibration response of nonuniform thin-walled beam structures exposed to external time-dependent excitation.

Introduction

THE modern combat aircraft is likely to operate in more hostile environments than in the past. In this sense, its structure has to be able to sustain during its mission, a variety of time-dependent loads induced e.g., by blast, fuel explosion, shock wave and sonic boom.

In view of the damaging effects these loads might have on structural integrity and survivability of flight vehicles, new concepts in the modeling, analysis, and control of their structural behavior have to be implemented. Moreover, other structural devices in the form of thin-walled beams, such as helicopter blades, robotic manipulator arms, as well as space booms, can also be dramatically affected by such loads.

As a result, in recent years there has been significant research on the integration of high-performance composites and smart materials to create intelligent/smart composite material structures.

The importance afforded to this problem was emphasized by the recent appearance of a number of comprehensive survey papers[1–4] that review in depth the state of the art on this issue and that provide an assessment of the achievements obtained so far in this area. It appears, however, that the problem of vibration control, by the use of both the structural tailoring and the optimal feedback control of a cantilevered thin-walled beam of nonuniform cross section, built up from anisotropic composite materials, has not yet been addressed.

Implementation of advanced composite materials in their construction requires an in-depth understanding of the implications of a number of nonclassical effects accompanying their use. Among these, the effects played by the elastic cross couplings induced by the directional properties of fiber-reinforced composite materials deserves further investigation.

An additional effect becoming more prominent with the increased use of advanced composite material structures is related to transverse shear flexibility. Although in general detrimental, its implications should be carefully investigated. Another feature whose implications should be considered in conjunction with the mentioned ones is related to the nonuniformity of the beam cross section.

In various contexts, the problem of the dynamic response of uniform cross section beams was addressed in Refs. 5–7. However, to the best of the authors' knowledge, no studies that investigate the implications of beam cross-sectional nonuniformity in the context of the problem considered here have been reported in the literature. In addition to cross-sectional nonuniformity, the considered thin-walled model incorporates material anisotropy, transverse shear, and warping inhibition. Their effects on the dynamic response to time-dependent external pulses will also be investigated.

To enhance the dynamic response characteristics of such structures when exposed to transient loadings, in addition to the anisotropy of constituent materials, advanced concepts of dynamic control must be developed and implemented. To control the oscillations induced by the action of blast pulses in the shortest possible time and with a minimum expenditure of energy, smart materials technology combined with that of optimal feedback control is used.

In spite of its practical importance, studies of the control of the dynamic response of cantilevered nonuniform thin-walled beams to transient pressure pulses via implementation of mentioned dual technology are virtually absent in the specialized literature. In specialized contexts, the problem was investigated in a number of papers.[5–7] The aim of the present paper is to supply pertinent information and reveal the efficiency of this dual control methodology as applied to the problem formulated earlier.

Basic Assumptions

This study uses the concept of single-cell, thin-walled beams of tapered planform and biconvex cross-sectional shape that incorporates the following features[8–11]: 1) transverse shear, 2) warping inhibition, 3) anisotropic properties of constituent materials, 4) doubly tapered geometrical features in both the horizontal and vertical

Presented as Paper 2000-1628 at the AIAA/ASME/ASCE/AHS/ASC Structures, Structural Dynamics Conference and Exhibit, Atlanta, GA, 3–6 April 2000; received 26 October 2000; revision received 4 June 2001; accepted for publication 30 December 2001.

*Assistant Professor, Department of Mechanical Engineering, Sungbuk-gu; nass@korea.ac.kr.

†Professor, Engineering Science and Mechanics Department; librescu@vt.edu.

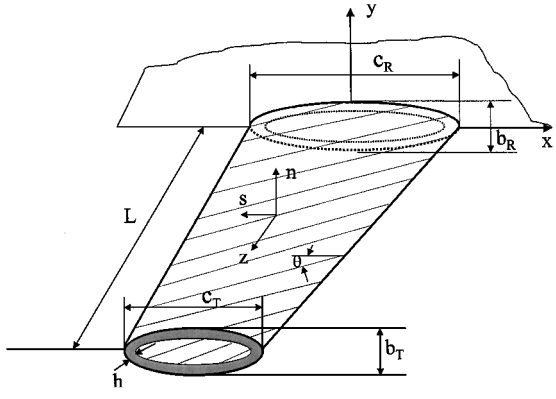

Fig. 1 Geometry of a doubly tapered thin-walled beam.

planes, 5) in-plane cross-sectional nondeformability, and 6) piezoactuators surface bonded on the top and bottom faces of the master structure and activated out-of-phase to induce a bending moment. Various actuator lengths from 10 to 100% of the beam span are considered. Assumption 4) requires the following linear distributions along the beam span of the chord $c(\eta)$ and height $b(\eta)$ of the midline cross-sectional profiles:

$$\begin{Bmatrix} c(\eta) \\ b(\eta) \end{Bmatrix} = [1 - \eta(1-\sigma)] \begin{Bmatrix} c_R \\ b_R \end{Bmatrix} \tag{1}$$

where $\sigma \equiv c_T/c_R = b_T/b_R$ defines the taper ratio, $0 \le \sigma \le 1$, where $\sigma = 1$ and 0 correspond to the extreme situations corresponding to the uniform and triangular beams, respectively; $\eta \equiv z/L$ is the dimensionless spanwise coordinate where L is the wing semispan, and the subscripts R and T refer to the wing root and tip cross section, respectively. Moreover, within the nonuniform beam model considered, the radius of curvature of the circular arc associated with the midline contour at section η along the beam span is expressed as

$$R(\eta) = [1 - \eta(1-\sigma)]R_R \tag{2}$$

where R_R is the radius of the circular arc of the root cross section profile. The wall thickness is assumed to be a constant one over the cross section and length of the structure.

The points on the beam cross sections are identified by the global coordinates x, y, and z, where z is the spanwise coordinate, and by the local coordinates s, n, and z (Fig. 1).

Kinematic Equations

In view of the preceding statements, the primary (or contour) warping function F_ω becomes a function of both s and η, that is,

$$F_\omega \equiv F_\omega(s,\eta) = \int_0^s [r_n(\bar{s},\eta) - \psi(\bar{s},\eta)]\,\mathrm{d}\bar{s} \tag{3}$$

where

$$\psi(s,\eta) = \frac{\oint r_n(\bar{s},\eta)\,\mathrm{d}\bar{s}}{h(s)G_{sz}(s,\eta)\oint \mathrm{d}\bar{s}/[h(\bar{s})G_{sz}(\bar{s},\eta)]} \tag{4}$$

is the torsional function, s is the arc length measured along the circumferential coordinate (whose origin is arbitrarily, but conveniently chosen), $\bar{s}$ is a dummy coordinate associated with the s coordinate, $\oint(\cdot)\,\mathrm{d}s$ is the integral along the closed midline contour, and $r_n(s,\eta) = x(s,\eta)\,\mathrm{d}y/\mathrm{d}s - y(s,\eta)\,\mathrm{d}x/\mathrm{d}s$ represents the perpendicular distance from a point on the reference longitudinal axis to the tangent at any point of the midsurface contour.[9] As is readily seen, in the case of the nonuniform thin-walled beam theory, ψ, F_ω, r_n, and $a(s,\eta)$ $[\equiv -y(s,\eta)\,\mathrm{d}y/\mathrm{d}s - x(s,\eta)\,\mathrm{d}y/\mathrm{d}s]$, which represents the perpendicular distance from a point on the refence longitudinal z axis to the normal at any point of the contour, are functions not only of the circumferential coordinate s, but of the spanwise η coordinate, as well. In addition, in Eq. (4), $G_{sz}(s,\eta)$ is the effective membrane shear stiffness.[11] The importance of including the variability of membrane shear stiffness in the expression of the torsional function was emphasized in Refs. 12 and 13.

In accordance with the mentioned assumptions, and to reduce the three-dimensional elasticity theory of beams to an equivalent one-dimensional one, the components of the displacement vector are expressed as[7,9]

$$u(x,y,z,t) = u_0(z,t) - y(s,z)\phi(z,t) \tag{5a}$$

$$v(x,y,z,t) = v_0(z,t) + x(s,z)\phi(z,t) \tag{5b}$$

$$w(x,y,z,t) = w_0(z,t) + \theta_x(z,t)\left[y(s,z) - n\frac{\mathrm{d}x}{\mathrm{d}s}\right] + \theta_y(z,t)\left[x(s,z) + n\frac{\mathrm{d}y}{\mathrm{d}s}\right] - \phi'(z,t)[F_\omega(s,z) + na(s,z)] \tag{5c}$$

where $F_\omega(s,z)$ and $na(s,z)$ play the role of primary and secondary warping functions, respectively, with n denoting the coordinate in the thickness direction. In addition,

$$\theta_x(z,t) = \gamma_{yz}(z,t) - v_0'(z,t) \tag{6a}$$

$$\theta_y(z,t) = \gamma_{xz}(z,t) - u_0'(z,t) \tag{6b}$$

where γ_{xz} and γ_{yz} are the transverse shear strains in the planes xz and yz, respectively, and the primes denote derivatives with respect to z. The quantities $u_0(z,t)$, $v_0(z,t)$, and $w_0(z,t)$ are the rigid-body translations along x, y, and z axes, respectively, and $\theta_x(z,t)$, $\theta_y(z,t)$, and $\phi(z,t)$ are the rotations about x and y axes and the twist about the z axis, respectively, and represent the unknowns quantities of the problem.

Consistent with Eqs. (5), the two-dimensional strain measures are $(\epsilon_{zz} \equiv \epsilon_{zz}^0 + n\epsilon_{zz}^n)$, $(\gamma_{sz} \equiv \tilde{\gamma}_{sz} + \tilde{\tilde{\gamma}}_{sz})$, and γ_{zn}. Their expression is

$$\epsilon_{zz}^0(s,z,t) = w_0' + x(s,z)\theta_y' + y(s,z)\theta_x' - F_\omega(s,z)\phi'' \tag{7a}$$

$$\epsilon_{zz}^n(s,z,t) = \theta_y'\frac{\mathrm{d}y}{\mathrm{d}s} - \theta_x'\frac{\mathrm{d}x}{\mathrm{d}s} - a(s,z)\phi'' \tag{7b}$$

$$\tilde{\gamma}_{sz}(s,z,t) = [u_0' + \theta_y]\frac{\mathrm{d}x}{\mathrm{d}s} + [v_0' + \theta_x]\frac{\mathrm{d}y}{\mathrm{d}s} \tag{7c}$$

$$\tilde{\tilde{\gamma}}_{sz}(s,z,t) = \psi(s,z,t)\phi' \tag{7d}$$

$$\gamma_{zn}(s,z,t) = [u_0' + \theta_y]\frac{\mathrm{d}y}{\mathrm{d}s} - [v_0' + \theta_x]\frac{\mathrm{d}x}{\mathrm{d}s} \tag{7e}$$

where ϵ_{zz}^0 and ϵ_{zz}^n are the axial strain components associated with primary and secondary warping, respectively; $\tilde{\gamma}_{sz}$ and $\tilde{\tilde{\gamma}}_{sz}$ are the tangential shear strains in the midsurface of the beam induced by transverse shear and twist, respectively; and γ_{zn} is the transverse shear strain component.

Governing System Involving Bending–Twist Elastic Coupling

The directional nature of fibrous composite materials offers the possibility to achieve exotic structural couplings that can be used to enhance the structural response in sensitive structures, such as aircraft wings, helicopter blades, robotic manipulator arms, etc. Implementation of structural/aeroelastic tailoring has revealed great promise toward improving static and dynamic response characteristics, preventing vibration resonance, and enhancing aeroelastic behavior of aircraft wing structure. For thin-walled composite beams, the possibility of generating desired elastic couplings via

the application of the tailoring technique was examined in a number of fundamental papers, such as Refs. 12 and 14. Among the couplings that can be induced via tailoring, one of the most beneficial for aircraft wing structures is the bending–twist cross coupling. In some earlier works in which a solid beam model was used, it was clearly revealed that this coupling can contribute to enhancing the structural/aeroelastic response behavior. As shown in Refs. 12 and 14, the ply-angle distribution with respect to the spanwise z axis inducing such a cross coupling is

$$\theta(x) = -\theta(-x), \qquad \theta(y) = -\theta(-y) \tag{8}$$

Two types of smart structure scenarios, cases 1 and 2, will be considered. In case 1, the piezoactuator consists of a single patch of finite size, distributed along the beam span, and in case 2, the piezoactuator is spread over the entire span of the beam. In both cases, the actuators are modeled as symmetric pairs mounted on the top and bottom external beam surfaces and activated out-of-phase.

As a result of the implementation of the ply-angle scheme defined by Eq. (8) and of the out-of-phase actuation, the governing system of the combined host–piezoactuator structure featuring the transverse bending–twist coupling, written in a unified form for both cases 1 and 2 is

$$\delta\phi\colon -\underline{(a_{66}\phi'')''} + (a_{73}\theta_x')' + (a_{77}\phi')' = (b_4 + b_5)\ddot{\phi} - \underline{((b_{10} + b_{18})\ddot{\phi}')'} \tag{9a}$$

$$\delta v_0\colon [a_{55}(v_0' + \theta_x)]' + \underline{(a_{56}\phi'')'} + p_y(z,t) = b_1\ddot{v}_0 \tag{9b}$$

$$\delta\theta_x\colon (a_{33}\theta_x')' + (a_{37}\phi')' - a_{55}(v_0' + \theta_x) - \underline{a_{56}\phi''} - \delta_p\hat{M}_x' = (b_4 + b_{14})\ddot{\theta}_x \tag{9c}$$

In addition, the solution of Eqs. (9) must satisfy the boundary conditions. For cantilevered beams these are, at $z = 0$,

$$\phi = 0 \tag{10a}$$

$$v_0 = 0 \tag{10b}$$

$$\theta_x = 0 \tag{10c}$$

$$\underline{\phi}' = 0 \tag{10d}$$

and the natural boundary conditions at $z = L$ are

$$\delta\phi\colon \underline{-(a_{66}\phi'')'} + a_{73}\theta_x' + a_{77}\phi' = -\underline{(b_{10} + b_{18})\ddot{\phi}'} \tag{11a}$$

$$\delta v_0\colon a_{55}(v_0' + \theta_x) + \underline{a_{56}\phi''} = 0 \tag{11b}$$

$$\delta\theta_x\colon a_{33}\theta_x' + a_{37}\phi' = \delta_S\hat{M}_x \tag{11c}$$

$$\delta\phi'\colon \underline{a_{66}\phi''} = 0 \tag{11d}$$

In Eqs. (9–11) the terms underscored by single and double solid lines are associated with the warping restraint and warping inertia, respectively.

In these equations, $a_{ij}\,(\equiv a_{ji})$ and b_i are stiffness and inertia coefficients, respectively. Because of the involvement in their expressions of primary and secondary warping functions, as well as of x and y, which exhibit circumferential and spanwise variations, these quantities become functions of the spanwise z coordinate. The expressions of these quantities are provided in the Appendix A.

Note that the stiffness terms $a_{37} = a_{73}$ and $a_{56} = a_{65}$ appearing in both the governing equations (9) and the boundary conditions [Eqs. (11)] are responsible for the coupling between bending and twist. These are referred to as bending–twist stiffness couplings.

In the same equations, the tracers δ_P and δ_S take the values 1 or 0, depending on whether the actuator is constituted of a piezopatch located along the beam span (case 1) implying $\delta_P = 1$ and $\delta_S = 0$ or is spread over the entire span of the beam (case 2), which requires $\delta_S = 1$ and $\delta_P = 0$. Whereas in the former case the piezoelectrically induced moment occurs in the governing equations, in the latter one it intervenes in the boundary conditions at the beam tip, and as a result the control is achieved via the piezoelectrically induced boundary bending moment (for example, see Refs. 15–17).

For the general case, the expression of the piezoelectrically induced bending moment is given by[15]

$$\hat{M}_x = \oint \sum_{k=1}^{\ell} \mathcal{E}_3^{(k)}\left(n_{(k^+)} - n_{(k^-)}\right) e_{31}^{(k)} R_{(k)}(s,z)\left[y\left(1 - \frac{A_{12}}{A_{11}}\right) + \frac{\mathrm{d}x}{\mathrm{d}s}\frac{B_{12}}{A_{11}}\right]\mathrm{d}s - \frac{1}{2}\oint_C \frac{\mathrm{d}x}{\mathrm{d}s}\sum_{k=1}^{\ell}\mathcal{E}_3^{(k)}\left(n_{(k^+)}^2 - n_{(k^-)}^2\right)e_{31}^{(k)} R_{(k)}(s,z)\,\mathrm{d}s \tag{12}$$

where ℓ is the number of piezoelectric layers, A_{ij} and B_{ij} are the two-dimensional stretching and stretching–bending stiffness quantities, respectively, and $R_{(k)}(s,z)$ is the two-dimensional step function. Equation (12) reveals that the piezoelectrically induced bending moment is proportional to the applied electric voltage $\mathcal{E}_3$. In the case of actuators symmetrically located through the beam thickness, the underlined term in Eq. (12) vanishes.

When the actuators are distributed over the entire beam span, $R(s,z) \Rightarrow R(s)$, and $\hat{M}_x$ becomes independent of the z coordinate. Consequently, its contribution appears in the boundary conditions only.

In contrast to this case, that is, when a discrete piezoelectric patch is involved, $\hat{M}_x \equiv \hat{M}_x(z)$, and its contribution appears solely in the governing equations.[5,6]

In the case of piezoactuators constituted of a patch, the global stiffness quantities a_{ij} and mass terms b_i can be cast as

$$a_{ij}(z) = \bar{a}_{ij} + \delta_P\hat{a}_{ij} + \delta_S\hat{\bar{a}}_{ij} \tag{13a}$$

$$b_i(z) = \bar{b}_i + \delta_P\hat{b}_i + \delta_S\hat{\bar{b}}_i \tag{13b}$$

where the terms denoted by an overbar and the circumflex are associated with the host structure and the piezoactuators, respectively. In different contexts their expressions are supplied in Refs. 5 and 6.

Because the applied electric field $\mathcal{E}_3$ can be expressed as $V(t)/h$, in the case of a piezopatch, an alternative representation for the piezoelectrically induced bending moment is obtained as

$$\hat{M}_x(z,t) = \mathcal{C}V(t)[Y(z - z_1) - Y(z - z_2)] \tag{14}$$

where $\mathcal{C}$ is a constant dependent on the mechanical and geometrical properties of the piezoactuator and host structure and $V(t)$ is the applied input voltage that is equal and opposite in sign in the upper and lower piezoactuators (out-of-phase actuation).

Solution of the Open/Closed-Loop Boundary-Value Problem

Thus far, displayed equations have been obtained via the application of Hamilton's variational principle.[8] In addition to this, Hamilton's variational principle can be used to devise a powerful solution methodology (see Ref. 17). This variational principle can be stated as

$$\int_{t_1}^{t_2}(\delta T - \delta V + \delta W)\,\mathrm{d}t = 0, \qquad \delta v_0 = \delta\theta_x = \delta\phi = 0 \quad \text{at} \quad t = t_1, t_2 \tag{15}$$

where T and V are the kinetic and strain energy, respectively, δW is the virtual work performed by the applied forces, and t_1 and t_2 are two arbitrary instants of time. Consistent with the ply-angle

distribution generating the bending–twist elastic coupling [Eq. (8)], the kinetic and strain energy quantities are

$$T = \frac{1}{2}\int_0^L \left[b_1\dot{v}_0^2 + (b_4+b_5)\dot{\phi}^2 + (b_{10}+b_{18})\,(\dot{\phi}')^2 + (b_{10}+b_{14})\dot{\theta}_x^2\right] \mathrm{d}z \tag{16a}$$

$$V = \frac{1}{2}\int_0^L \left[a_{33}(\theta_x')^2 + a_{55}\theta_x^2 + a_{66}(\phi'')^2 + a_{77}(\phi')^2 + a_{55}(v_0')^2 + 2a_{37}\theta_x'\phi' + 2a_{55}v_0'\theta_x + 2a_{56}\theta_x\phi'' + 2a_{56}v_0''\phi''\right] \mathrm{d}z \tag{16b}$$

For computational reasons, it is necessary to discretize the boundary-value problem, which amounts to representing v_0, θ_x, and ϕ by means of series of space-dependent trial functions multiplied by time-dependent generalized coordinates. The discretization can be more conveniently performed directly via the extended Hamilton's principle [Eq. (15)]. To this end, we express the displacements v_0, θ_x, and ϕ as follows:

$$v_0(z,t) = \boldsymbol{V}^T(z)\boldsymbol{q}_v(t) \tag{17a}$$

$$\theta_x(z,t) = \boldsymbol{R}^T(z)\boldsymbol{q}_R(t) \tag{17b}$$

$$\phi(z,t) = \boldsymbol{S}^T(z)\boldsymbol{q}_s(t) \tag{17c}$$

where

$$\boldsymbol{V} = [V_1, V_2, \ldots, V_N]^T \tag{18a}$$

$$\boldsymbol{R} = [R_1, R_2, \ldots, R_N]^T \tag{18b}$$

$$\boldsymbol{S} = [S_1, S_2, \ldots, S_N]^T \tag{18c}$$

are the vectors of trial functions, whereas

$$\boldsymbol{q}_v(t) = \left[q_1^v, q_2^v, \ldots, q_N^v\right]^T \tag{19a}$$

$$\boldsymbol{q}_R(t) = \left[q_1^R, q_2^R, \ldots, q_N^R\right]^T \tag{19b}$$

$$\boldsymbol{q}_S(t) = \left[q_1^S, q_2^S, \ldots, q_N^S\right]^T \tag{19c}$$

are vectors of generalized coordinates, and the superscript T is the transpose operation of a matrix.

Inserting Eqs. (17) into Eqs. (16), we can express the kinetic and potential energies in discrete form as

$$T = \tfrac{1}{2}\dot{\boldsymbol{q}}^T\boldsymbol{M}\dot{\boldsymbol{q}} \tag{20a}$$

$$V = \tfrac{1}{2}\boldsymbol{q}^T\boldsymbol{K}\boldsymbol{q} \tag{20b}$$

where $\boldsymbol{M}$ and $\boldsymbol{K}$ are the mass and stiffness matrices, respectively, of the structure considered in its entirety, that is, of the host and piezoactuators. The expressions of these quantities are supplied in Ref. 8.

Performing the integration with respect to the spanwise z coordinate and with respect to time, and keeping in mind Hamilton's condition, from Eq. (15), one obtains the discrete equations of motion

$$\boldsymbol{M}\ddot{\boldsymbol{q}} + \boldsymbol{K}\boldsymbol{q} = \boldsymbol{Q} - \boldsymbol{F}\boldsymbol{u} \tag{21}$$

where $\boldsymbol{u}$ is the vector of the control input. In addition,

$$\boldsymbol{Q} = \int_0^L p_y\boldsymbol{V}\,\mathrm{d}z \tag{22a}$$

$$\boldsymbol{F} = [R_i(z_2) - R_i(z_1)] \tag{22b}$$

are the generalized vector of time-dependent external excitations and the vector of piezoelectrically induced bending moment, respectively.

When the state vector is defined as $\boldsymbol{x}(t) = [\boldsymbol{q}^T(t), \dot{\boldsymbol{q}}^T(t)]^T$ and the identity $\dot{\boldsymbol{q}} = \dot{\boldsymbol{q}}$ is added, Eq. (21) can be cast in state-space form (for example, Refs. 5 and 6),

$$\dot{\boldsymbol{x}}(t) = \boldsymbol{A}\boldsymbol{x}(t) + \boldsymbol{B}\boldsymbol{Q}(t) + \boldsymbol{W}\boldsymbol{u}(t) \tag{23}$$

where

$$\boldsymbol{A} = \begin{bmatrix} \boldsymbol{0} & \boldsymbol{I} \\ -\boldsymbol{M}^{-1}\boldsymbol{K} & \boldsymbol{0} \end{bmatrix} \tag{24a}$$

$$\boldsymbol{B} = \begin{bmatrix} \boldsymbol{0} \\ \boldsymbol{M}^{-1} \end{bmatrix} \tag{24b}$$

$$\boldsymbol{W} = \begin{bmatrix} \boldsymbol{0} \\ -\boldsymbol{M}^{-1}\boldsymbol{F} \end{bmatrix} \tag{24c}$$

Optimal Feedback Control

For the optimal control problem, given an initial state $\boldsymbol{x}(t_0)$, the goal is to find a control vector $\boldsymbol{u}(t)$ defined on $t \in [t_0,\ t_f]$ that drives the state $\boldsymbol{x}(t_0)$ to the desired final state $\boldsymbol{x}(t_f)$ in such a way that a selected performance index is minimized. In a number of recent works (for example, Ref. 18) it was argued that the standard algorithms aimed at optimally controlling the structures exposed to time-dependent external excitations do not include the time-dependent external load in the performance index to be minimized. Incorporation of this term results in a time-dependent performance index that has to be minimized at any instant of time, wherefrom comes the terminology of instantaneous optimal control afforded to this control algorithm.

When the instantaneous optimal control concept is adopted, and the approach of Refs. 5 and 6 is followed, the augmented performance index including the constraint equation (23) is

$$J_a = \frac{1}{2}\boldsymbol{x}^T(t_f)\boldsymbol{T}\boldsymbol{x}(t_f) + \int_{t_0}^{t_f}\left\{\frac{1}{2}\,(\boldsymbol{x}^T\boldsymbol{Z}\boldsymbol{x} + \boldsymbol{u}^T\boldsymbol{R}\boldsymbol{u}) + \boldsymbol{k}^T[\boldsymbol{A}\boldsymbol{x}(t) + \boldsymbol{W}\boldsymbol{u}(t) + \boldsymbol{B}\boldsymbol{Q}(t) - \dot{\boldsymbol{x}}]\right\}\mathrm{d}t \tag{25}$$

in which $\boldsymbol{k}(t)$ is the vector of Lagrangian multipliers (referred to as the costate), $\boldsymbol{Z}$ and $\boldsymbol{R}$ are positive semidefinite and positive definite weighting matrices, respectively, $\boldsymbol{T}$ is the positive semidefinite weighting matrix associated with the error in the terminal state at $t = t_f$, and $\boldsymbol{u}^T = [u_1, \ldots, u_m]$, where m is the number of piezoactuator patches. For large weighting matrix $\boldsymbol{Z}$, the response is small, and the required active control $\boldsymbol{u}(t)$ will be large. As a result, suitable $\boldsymbol{Z}$ and $\boldsymbol{R}$ that provide a desired balance between the state variable responses and control efforts, while satisfying performance requirements and constraints, should be determined. The approach of the optimal control based on Eq. (25) is referred to as the instantaneous optimal control.

As shown in Refs. 5 and 6, the linear optimal control law can be expressed as

$$\boldsymbol{u}(t) = -\boldsymbol{R}^{-1}\boldsymbol{W}^T\boldsymbol{P}(t)\boldsymbol{x}(t) - \boldsymbol{R}^{-1}\boldsymbol{W}^T\boldsymbol{d}(t) \tag{26}$$

where $\boldsymbol{P}(t)$ and $\boldsymbol{d}(t)$ are the solutions of the equations

$$\dot{\boldsymbol{P}} = -\boldsymbol{Z} - \boldsymbol{A}^T\boldsymbol{P} - \boldsymbol{P}\boldsymbol{A} + \boldsymbol{P}\boldsymbol{W}\boldsymbol{R}^{-1}\boldsymbol{W}^T\boldsymbol{P} \tag{27}$$

$$\dot{\boldsymbol{d}} = -(\boldsymbol{A}^T - \boldsymbol{P}\boldsymbol{W}\boldsymbol{R}^{-1}\boldsymbol{W}^T)\boldsymbol{d} - \boldsymbol{P}\boldsymbol{B}\boldsymbol{Q} \tag{28}$$

To determine $\boldsymbol{P}(t)$ and $\boldsymbol{d}(t)$ that appear in the optimal control law [Eq. (26)], these two equations have to be integrated backward in time from t_f to t_0 in conjunction with the conditions at $t = t_f$,

$$\boldsymbol{P}(t_f) = \boldsymbol{T} \tag{29a}$$

$$\boldsymbol{d}(t_f) = \boldsymbol{0} \tag{29b}$$

When the external pressure pulse is disregarded in the augmented performance index, the optimal control law is simplified. If, in addition, the terminal time t_f approaches infinity, the Riccati gain matrix $\boldsymbol{P}(t)$ becomes a constant matrix $\boldsymbol{P}_c$, which is the solution to the nonlinear algebraic Riccati equation,

$$\boldsymbol{A}^T\boldsymbol{P}_c + \boldsymbol{P}_c\boldsymbol{A} - \boldsymbol{P}_c\boldsymbol{W}\boldsymbol{R}^{-1}\boldsymbol{W}^T\boldsymbol{P}_c + \boldsymbol{Z} = \boldsymbol{0} \tag{30}$$

Consistent with the steady-state control, the optimal control law is given by

$$\boldsymbol{u}(t) = -\boldsymbol{G}^T\boldsymbol{x}(t) \tag{31}$$

where the optimal gain matrix is

$$\boldsymbol{G} = \boldsymbol{R}^{-1}\boldsymbol{W}^T\boldsymbol{P} \tag{32}$$

As mentioned, in the case of piezoactuators spread over the entire span of the beam, the piezoelectrically induced bending moment $\hat{M}_x$ appears in the boundary condition at $z = L$ only. Its expression is

$$\hat{M}_x = \boldsymbol{F}u, \qquad u = \mathcal{C}V(t) \tag{33a}$$

$$\boldsymbol{F} = R_i'(L) \tag{33b}$$

In addition to this modification, the mass and the stiffness are obtained by setting $\delta_P = 0$ and $\delta_S = 1$ in Eqs. (9) and (11).

In this work both methods, that is, the instantaneous control and the linear quadratic regulator (LQR) based on the solution of Riccati's equation [Eq. (30)] will be applied.

Sensor Output and Power Consumption

One assumes that the piezoelectric elements can be employed concurrently for sensing and actuation. For sensing operation, setting $\mathcal{E}_3 = 0$, the electric displacement is given by

$$D_3 = e_{31}\epsilon_{zz} \tag{34}$$

and considering the strain–displacement relationship in the piezofilm, it follows that

$$D_3 = -e_{31}y(s)\theta_x' \tag{35}$$

The electric charge due to the direct effect of the PZT material can be found through integration of the electric displacement over the corresponding sensor area,

$$q_p(t) = \int_A D_3\,\mathrm{d}A = -\int\!\!\int e_{31}y(s)\theta_x'\,\mathrm{d}s\,\mathrm{d}z \tag{36}$$

The limits of integration in Eq. (36) depend on the sensor–patch configuration.

The voltage across the piezoelectric sensor can be found by dividing the charge developed in the sensor by the sensor's capacitance C_p (Ref. 19)

$$V_p(t) = q_p(t)/C_p \tag{37}$$

where C_p depends on the patch area A_p, thickness h^a, and the permittivity of the piezoelectric material ξ_{33}^p, according to[19]

$$C_p = \xi_{33}^p A_p \big/ h^a \tag{38}$$

As a result, the sensor electric current output results as

$$I_p = \frac{\mathrm{d}q_p(t)}{\mathrm{d}t} = -\int e_{31}y(s)\dot{\theta}_x'\,\mathrm{d}s\,\mathrm{d}z$$

$$= -\int e_{31}y(s)[\dot{\theta}_x(z_2) - \dot{\theta}_x(z_1)]\,\mathrm{d}s \tag{39}$$

Furthermore, one assumes that the actuator voltage required for vibration suppression is proportional to the sensor output voltage (see Refs. 7 and 20). Accordingly, the electric power consumption during vibration control can be obtained as the product of the sensor output voltage and current as $P = V_p I_p$.

Blast Pulses

The case of the step pulse, explosive blast, sonic boom, and rectangular and sine overpressure signatures will be considered. As was clearly established, the blast wave reaches the peak value in such a short time that the structure can be assumed to be loaded instantly and uniformly in the chordwise and spanwise directions. The overpressure associated with the blast pulses can be described in terms of the modified Friedlander exponential decay equation as (for example, see Ref. 21):

$$p_y(s, z, t)[\equiv p_y(t)] = P_m(1 - t/t_p)\exp(-a't/t_p) \tag{40}$$

where the negative phase of the blast is included. In Eq. (40), P_m is the peak reflected pressure in excess of the ambient one, t_p is the positive phase duration of the pulse measured from the time of impact of the structure, and a' is a decay parameter that has to be adjusted to approximate the overpressure signature from the blast tests. As could be inferred, the triangular explosive load may be viewed as a limiting case of Eq. (40), occurring for $a'/t_p \to 0$. The sonic-boom wave signature as considered in the present study can be described as

$$p_y(s, z, t) \equiv p_y(t) = \begin{cases} P_m(1 - t/t_p) & \text{for} \quad 0 < t < rt_p \\ 0 & \text{for} \quad t > rt_p \end{cases} \tag{41}$$

where r is the extent of the negative phase of the pulse. The step pulse is defined as $p_y(s, z, t) = p_y(t) = P_m$ for $t \geq 0$.

In addition, the cases of the sine and rectangular pressure pulses described as

$$p_y(s, z, t)[\equiv p_y(t)] = \begin{cases} \left.\begin{matrix} P_m \sin \pi t/t_p, & 0 \leq t \leq t_p \\ 0, & t > t_p \end{matrix}\right\} \text{sine pulse} \\ \left.\begin{matrix} P_m, & 0 \leq t \leq t_p \\ 0, & t > t_p \end{matrix}\right\} \text{rectangular pulse} \end{cases} \tag{42}$$

will also be considered in the study of the dynamic response.

Results and Discussion

The displayed numerical results are based on thin-walled beams of symmetric biconvex cross section profile (Fig. 1). The beam dimensions, unless indicated to the contrary, are $L = 80$ in. and $h = 0.4$ in. For numerical simulations one considers that the host structure is constructed of a graphite–epoxy composite material. Its on-axis elastic properties are supplied in Appendix B. The piezopatch manufactured of PZT-4 piezoceramic is located as indicated in Fig. 2, where also its fixed dimensions are supplied. For its properties, see Ref. 15. Throughout these results, unless otherwise specified $P_m = 50$ lb/L.

Before presenting the results emphasizing the implications of various effects that involve the structural model and the performance of the adopted control methodology (Fig. 3), the fast convergence

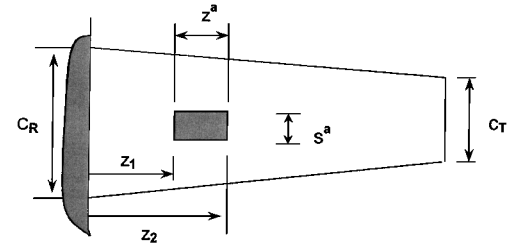

s^a=3.5in(0.089m) t^a=0.00787in(0.0002m)

Fig. 2 Distribution of the piezopatch actuator.

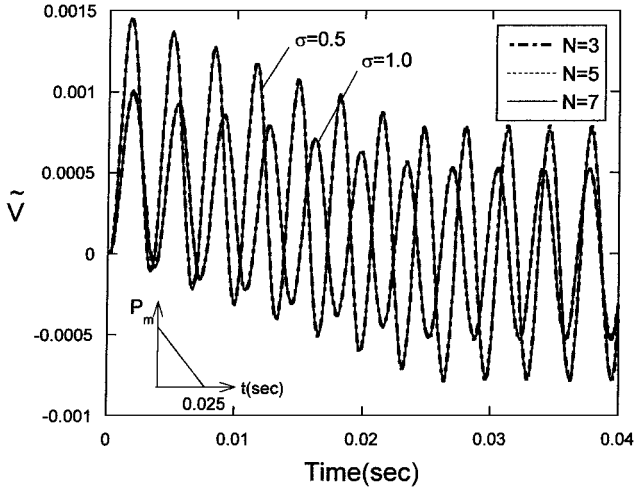

Fig. 3 Speed of convergence of the solution methodology that is related to the deflection time history: $L = 30$ in. and unshearable beam model.

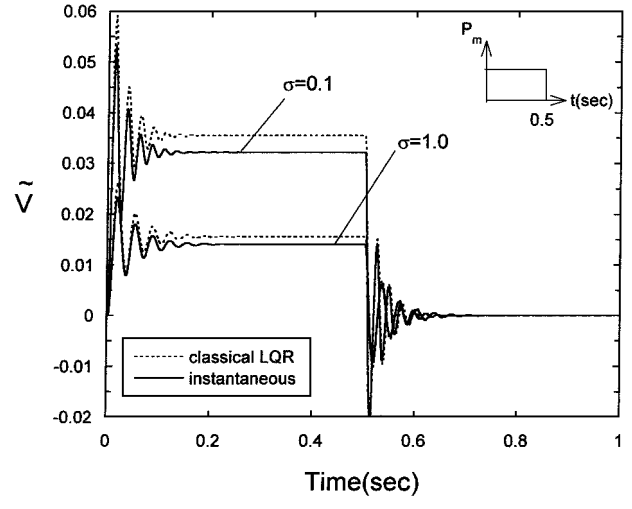

Fig. 4 Dimensionless transverse deflection time history of the beam tip subjected to a rectangular pulse (inset) for two values of σ and for classical and instantaneous optimal control: $L = 30$ in., $\theta = 45$ deg, $z^a = (0.2\text{–}0.1)L$, and nonshearable and free warping model.

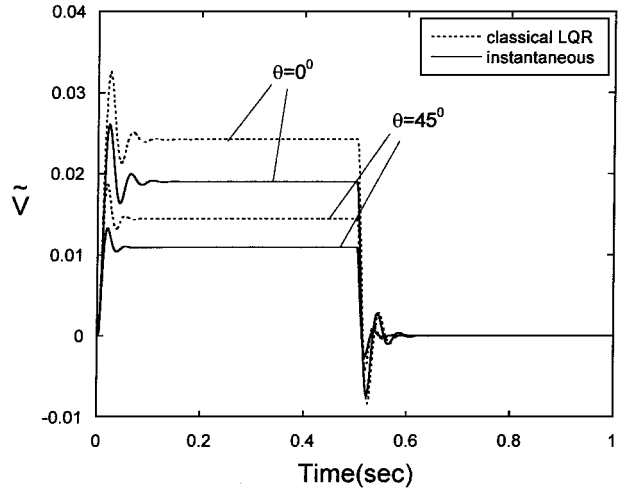

Fig. 5 Implications of ply angle and of two optimal control methodologies for the dimensionless transverse deflection time history of the beam tip subjected to a rectangular pressure pulse (see inset Fig. 3): $L = 30$ in., $\sigma = 1$, and nonshearable and free warping wing model.

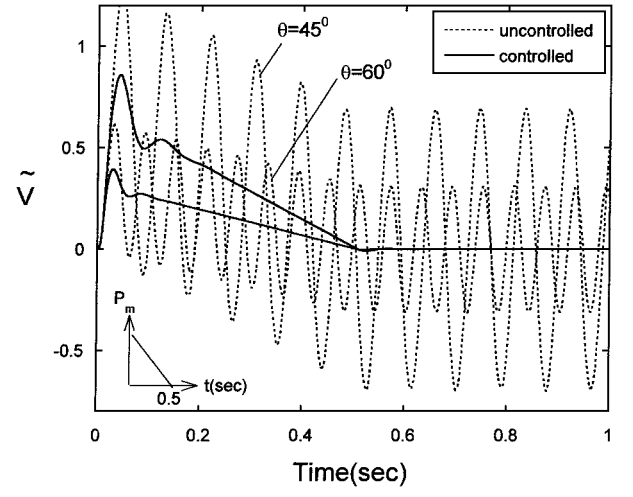

Fig. 6 Implication of the ply angle for the open/closed-loop dimensionless deflection time history of the beam tip subjected to a blast pulse: $\sigma = 0.1$ and $z^a = (0.2\text{–}0.1)L$.

of the implemented solution methodology is displayed. In Fig. 3, for the sake of illustration, only the open-loop transversal deflection $\tilde{V}(\equiv V/L)$ time history of the tip beam cross section, exposed to a blast pulse (represented in the inset) is shown. Both uniform and tapered beams are considered in the formulation. $N = 3$, 5, and 7 denotes the number of trial functions used in Eqs. (18). In addition, the classical, unshearable beam model was considered. Figures 4 and 5 show the time history of the normalized deflection $\tilde{V}$ of the beam tip when classical LQR and instantaneous optimal control methodologies are applied. Moreover, the effects of the ply angle and taper ratio are also put into evidence.

From Figs. 4 and 5, the following conclusions are emerging: 1) The classical LQR optimal control provides an upper bound of the deflection amplitude as compared to that resulting in the case of the instantaneous one. The relative percentage overestimation of the deflection amplitude resulting in the case of the adoption of the classical LQR as compared to the instantaneous one is 12.5% for $\sigma = 1$ and 11% for $\sigma = 0.1$. Although these results have been outlined for the case of a beam exposed to a rectangular pressure pulse, the described trend also remains valid for different pressure signature profiles. 2) The increase of the ply angle inducing an increase of the bending stiffness results in a decrease of the deflection amplitudes. The same effect results when the beam taper ratio decreases (implying an increase of σ). At the same time, with the increase of the bending stiffness resulting from the increase of the ply angle, the differences between the predictions based on classical and instantaneous optimal control methodologies start to diminish.

In Figs. 6 and 7, the effects of the ply-angle and beam taper ratio on the normalized open/closed-loop transverse deflection time history of the beam tip are highlighted. In this case, the beam is exposed to a triangular blast pulse shown in the inset of Fig. 6.

For the unactivated beam, it appears evident that the increase of the ply angle and taper ratio results in a decay of the deflection amplitude in both the forced motion, that is, the motion in the time range $0 \leq t \leq 0.5$ s, and free motion, that is, when $t > 0.5$ s, regimes. For the activated beam, excepting the region of the forced motion regime where the increase of the ply angle and taper ratio yield a dramatic decrease of the deflection amplitude, in the free motion regime, for any considered ply angle and taper ratio, the motion is completely suppressed.

Related to the implications of the ply angle and taper ratio on the beam response, the same trend as in Fig. 6 also appears to be valid for the twist motion at the beam tip (Fig. 8), when the beam is exposed to a triangular blast pulse as shown in the inset.

In Fig. 9a, the implications of the piezoactuator size and taper ratio for the transversal deflection time history of the beam tip when subjected to a step pulse are shown.

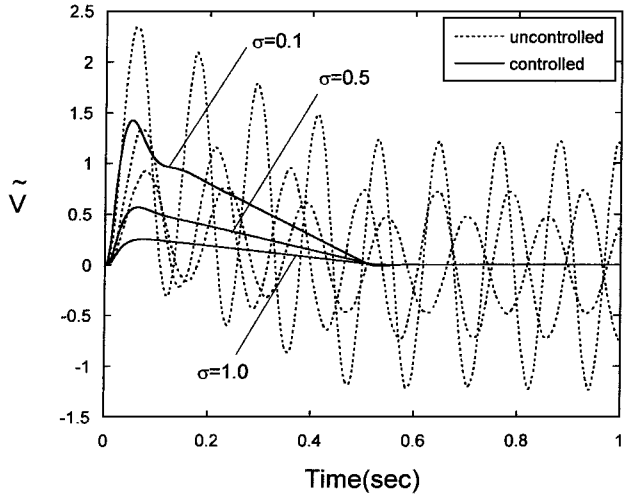

Fig. 7 Implication of the taper ratio for the open/closed-loop dimensionless deflection time history of the beam tip subjected to a blast pulse (inset of Fig. 5): $\theta = 0$, $z^a = (0.2\text{–}0.1)L$, and unshearable and free warping beam model.

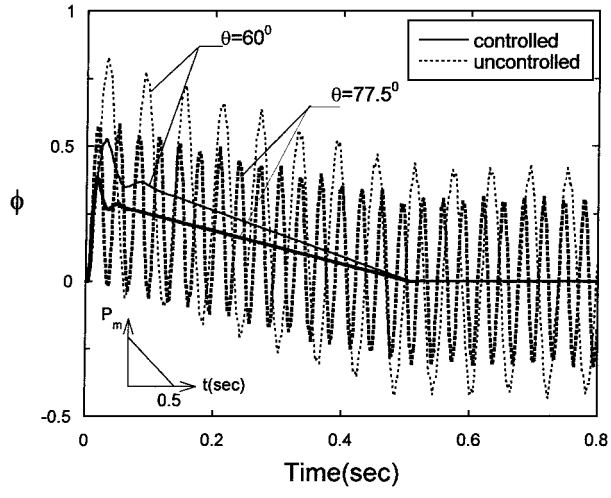

Fig. 8 Implication of the ply angle on the open/closed-loop twist time history of the beam tip subjected to a blast pulse: $z^a = (0.2\text{–}0.1)L$, $\sigma = 0.1$, and unshearable and free warping beam model.

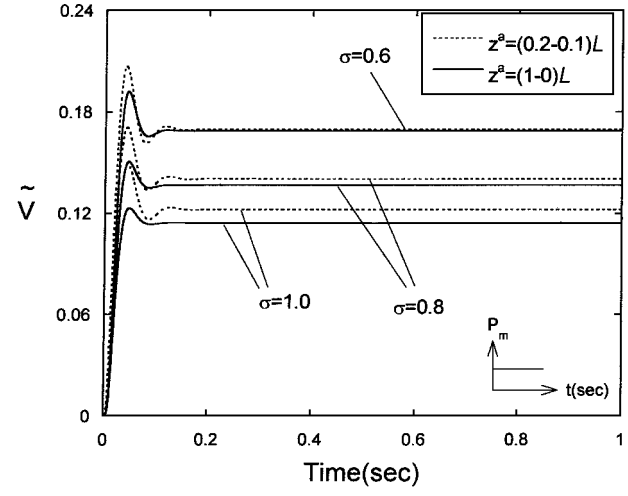

Fig. 9a Effects of beam taper and piezoactuators size on the deflection time history at the beam tip when subjected to a step pulse: $\theta = 60$ deg.

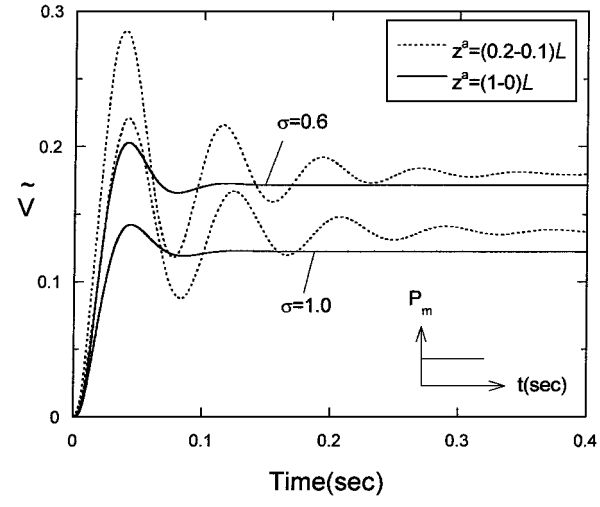

Fig. 9b Counterpart of Fig. 9a for a voltage costraint, $V_{\max} = 300$ V.

The results reveal the following:

1) The increase of σ toward $\sigma = 1$, that is, toward the uniform beam, results in a decrease of the deflection amplitude.

2) For uniform beams ($\sigma = 1$), the effectiveness of the piezopatch actuator appears to be lower than that of the full span actuator. However, for tapered beams, this trend changes, in the sense that the effectiveness of the piezopatch actuator becomes equivalent to that of the full span actuator. Related to this change in trend, one may conjecture that this is because the width of the actuators is constant, and for the tapered beam, the control efficiency is higher than for the uniform beam counterpart.

3) Although for the present case the adopted optimal control methodology appears to be highly efficient toward containing the motion, the results reveal that it is not able to suppress it. This implies that in the case of permanent excitations (such as those related with a step pulse) more powerful control methodologies should be adopted.

Figure 9b represents the counterpart of Fig. 9a, for the case when a constraint on the maximum voltage, that is, $V_{\max} = 300$ V, is imposed. Although the results reveal similar global trends as in Fig. 9a, several small differences should be remarked: 1) In both cases of considered piezoactuators, the voltage constraint is paid by a slight increase of the deflection amplitude at which the motion is contained, as compared to the case of the unconstrained voltage. 2) During the first instances of motion and irrespective of the taper ratio, the discrete piezoactuator is less effective toward containing the motion than in the case of a voltage constraint. However, this conclusion is not applicable to the full space actuator.

In Fig. 10, open/closed-loop normalized transverse deflection amplitude time histories of the beam tip exposed to a sinusoidal pulse, as affected by the aspect ratio $AR(\equiv 2L/c)$, are shown. As expected, the amplitude of oscillations is strongly influenced by the beam aspect ratio, in the sense that its increase yields an increase of deflection amplitudes. For the activated beam, however, the influence of the beam aspect ratio is experienced mainly in the forced motion regime, that is, for $t \leq 0.167$ s, whereas in the free motion regime, that is, for $t > 0.167$ s, the motion appears to be suppressed, irrespective of the beam aspect ratio.

In Fig. 11, for the same sinusoidal pulse, the effects of the piezoactuator size and beam taper ratio on the open/closed-loop deflection at the beam tip are highlighted. The results reveal that the increase in size of the piezopatch yields a relatively modest decrease of the deflection amplitudes in the forced motion regime, whereas in the free motion regime its effect becomes immaterial. As concerns the effect of taper ratio, its implications are similar to those already emphasized. The results related to the twist time history of the beam tip under conditions identical to those valid in Figs. 10 and 11 reveal a similar trend. These results are not displayed here.

Figures 12a and 12b show the effects on the deflection and twist time history, respectively, to a sonic boom, of the location along the beam span of a piezopatch of fixed size. The results reveal both the high efficiency of the application of the piezoactuation toward suppressing the oscillatory motion, as well as the strong influence played by the location of the piezopatch.

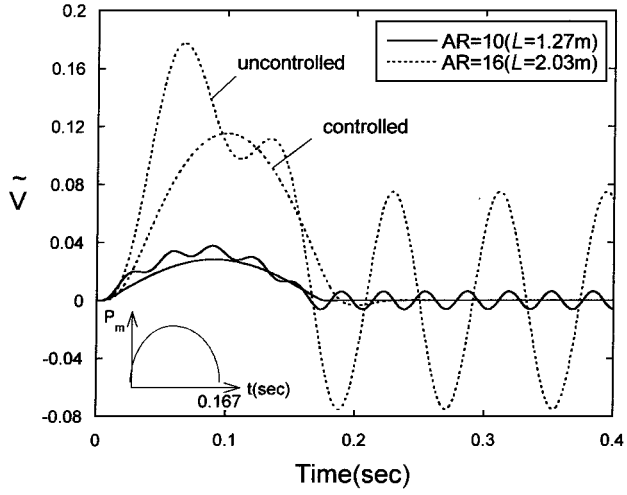

Fig. 10 Implication of the beam aspect ratio on the open/closed-loop dimensionless deflection time history of the beam tip: sinusoidal pulse, $z^a = (1-0)L$, $\theta = 60$ deg, and $\sigma = 1$.

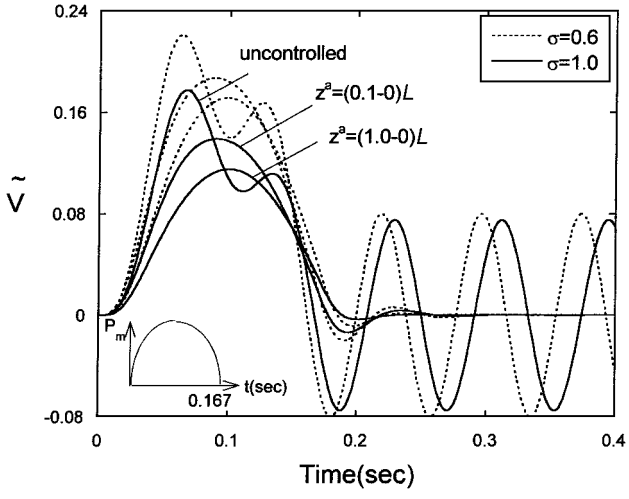

Fig. 11 Implication of taper ratio on open/closed dimensionless deflection time history of the beam tip: sinusoidal pulse, $\theta = 60$ deg, and $z^a = (1-0)L$.

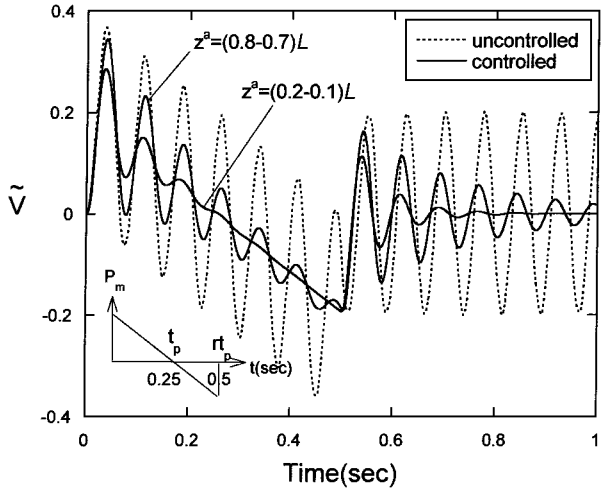

Fig. 12a Implications of the piezopatch location on open/closed-loop transverse deflection time history of the beam tip, subjected to a sonic boom: $\sigma = 0.5$, $\theta = 60$ deg, and unshearable and free warping beam model.

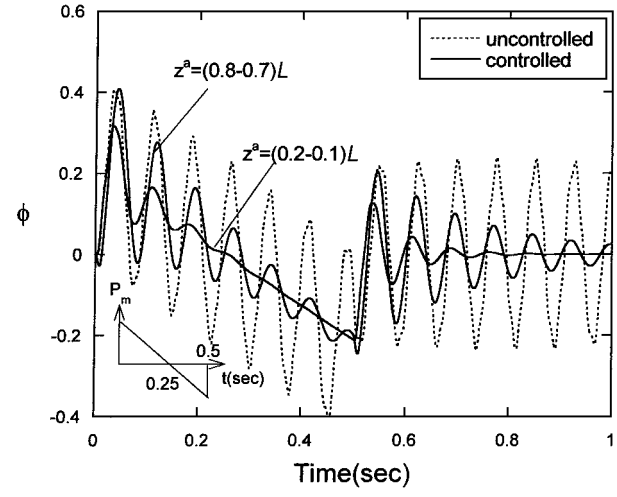

Fig. 12b Counterpart of Fig. 12a for the twist time history.

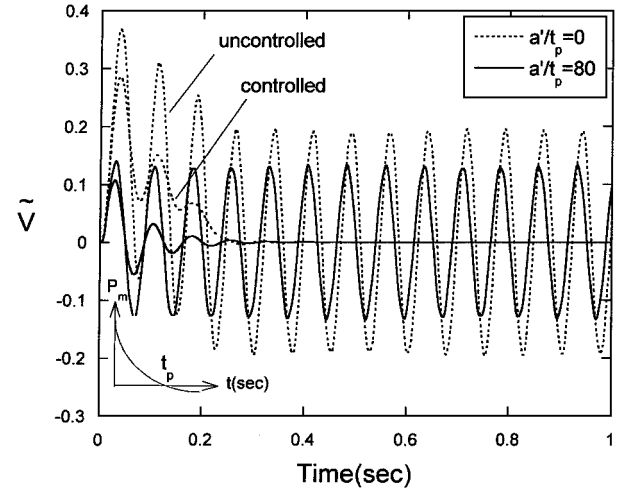

Fig. 13 Implications of the decay parameter a'/t_p of the blast pulse on the dimensionless deflection time history of the beam tip: $\sigma = 0.5$, $\theta = 60$ deg, $t_p = 0.25$ s, and unshearable and free warping beam model.

It is clearly seen that for the cantilevered beam the best location of the patch is toward the beam root. Results related to the twist time history of the beam tip (Fig. 12b) reflect a trend similar to that of the transversal deflection time history. Note that the involved twist motion is a result of the bending–twist elastic coupling. Although the present control appears to be rather effective also with respect to the twist motion, the use of piezoactuator elements skewed with respect to the beam longitudinal axis is likely to enhance the control of torsional modes (for example, see Ref. 22).

In Fig. 13, the influence of the shape factor of the explosive blast pulse, a'/t_p, on the transversal deflection time history of the beam is shown. The results reveal that, in the case of the unactivated beam, the triangular pulse ($a'/t_p = 0$) that is the most severe explosive-type pulse results in the largest deflection amplitude.

However, with the increase of a'/t_p, which implies a decay of the severity of the pulse, the transversal deflection time-history amplitude of the unactivated beam drops in magnitude. For the activated beam, with the exception of the forced motion regime where the parameter a'/t_p plays at a lower scale, an effect similar to that of the unactivated beam, in the free motion regime its influence is immaterial, and the motion is totally suppressed, irrespective of the value of a'/t_p.

In Fig. 14, the influence of the size of the patch that is located near the root of the cantilevered beam on the deflection time history of the beam tip exposed to an explosive pressure pulse that also includes its negative phase is shown. The results reveal that the piezoactuator of larger size is slightly more effective to contain the displacement in

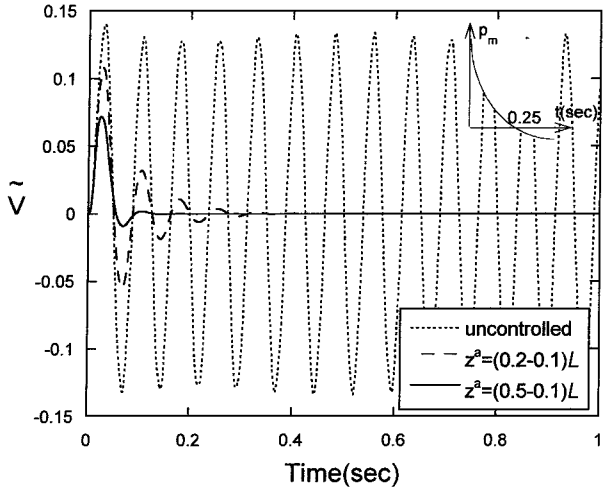

Fig. 14 Implications of the piezopatch size on deflection time history of the beam tip subjected to a blast pulse whose negative phase is included: $a'/t_p = 80$, $t_p = 0.25$, $\sigma = 0.5$, and $\theta = 60$ deg.

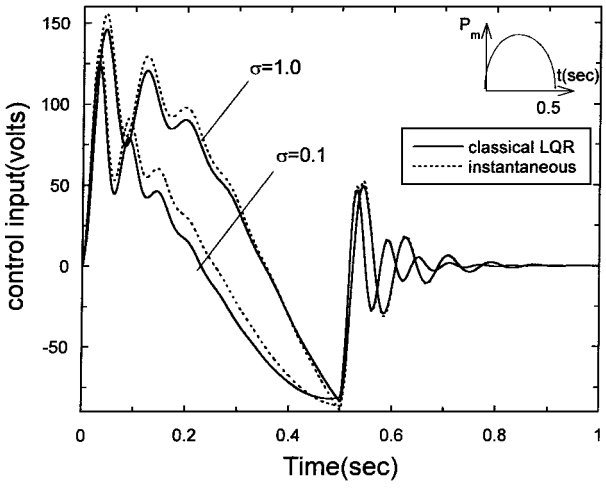

Fig. 15 Implications of beam taper ratio and of the two optimal control methodologies on control input voltage time history of a beam tip subjected to a sinusoidal pulse: $\theta = 60$ deg, and $z^a = (0.2\text{–}0.1)L$.

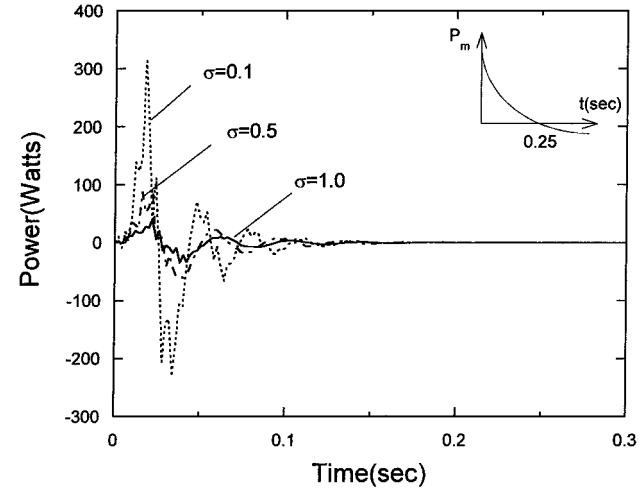

Fig. 16 Implications of beam taper ratio on the consumed power time history of a beam subjected to a blast pulse: $L = 30$ in., $\theta = 45$ deg, $z^a = (0.2\text{–}0.1)L$, $t_p = 0.25$ s, and $a'/t_p = 80$.

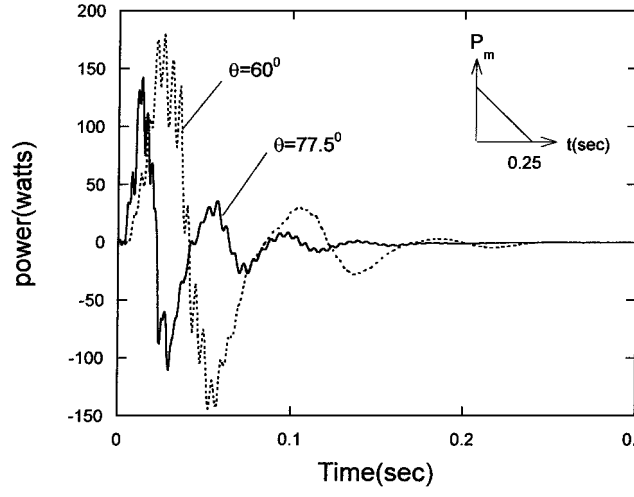

Fig. 17 Implications of the ply angle on the consumed power time history of the beam tip when subjected to a blast load: $\sigma = 0.5$ and $z^a = (0.2\text{–}0.1)L$.

the forced motion regime. However, in the free motion regime, there is no difference in their efficiency, and in both cases, the motion is completely suppressed.

In Fig. 15, the implications of the two optimal control methodologies, namely, of the classical LQR and the instantaneous one, and of the beam taper ratio on the control input time history of the beam tip exposed to a sinusoidal pulse is shown. The results reveal the following: 1) In the forced motion regime for the uniform beam ($\sigma = 1$), which is stiffer than its tapered beam counterpart, a higher voltage is needed to contain the vibrations. However, in the free motion regime, that is, for $t > 0.5$ s, the influence of the taper ratio diminishes dramatically and tends to disappear as time unfolds. 2) In the case of the forced motion regime for tapered beams ($\sigma = 0.1$) that are more flexible than their uniform counterparts, the instantaneous optimal control methodology yields larger voltages than those resulting in the case of the classical LQR control methodology. In contrast to this trend, for uniform beams ($\sigma = 1$), the voltages predicted by the two optimal control methodologies are rather close each other. However, in the free motion regime, that is, for $t > 0.5$ s, the differences in the control input predictions by the two control methodologies become completely immaterial, irrespective of the beam taper ratio.

In Fig. 16 the effect played by the taper ratio on the electrical power used for the optimal oscillation control of the beam exposed to a blast pulse is shown. The supplied results show that, as the beam becomes more uniform, implying $\sigma \to 1$, that is, when its stiffness increases, the electrical power tends to decay. However, in the free motion regime, where the motion is suppressed, there is no difference in power, irrespective of the taper ratio.

In Fig. 17, the effects of the ply angle on the electrical power time history of a beam subjected to a blast load are shown. The results reveal that with the increase of the ply angle, which yields an increase of the beam stiffness, a decrease of the electrical power results.

In Fig. 18 the total energy time history (that is of strain energy plus the kinetic energy) of the beam when exposed to a blast load, for both the activated and unactivated cases, is shown. The results reveal that for the activated beam, in the free-motion regime where the motion is suppressed, the total energy is reduced to zero, whereas for the unactivated case, due to the absence of the structural damping, the total energy is uniform in time. The results also reveal that the size of piezoactuator plays a small role in the forced-motion regime, in the sense that, corresponding to the larger size piezoactuator, the amplitude of the total energy is slightly lower than that corresponding to lower size actuators. However, in the free motion regime, the influence of the piezoactuator size on the total energy is completely immaterial.

Throughout the numerical simulations presented, the mass and stiffness of actuators were included in their global expressions. It is, however, an usual practice to discard their effect on the global mass and stiffness quantities. A comparison of results obtained by including and ignoring the mass and stiffness of actuators should

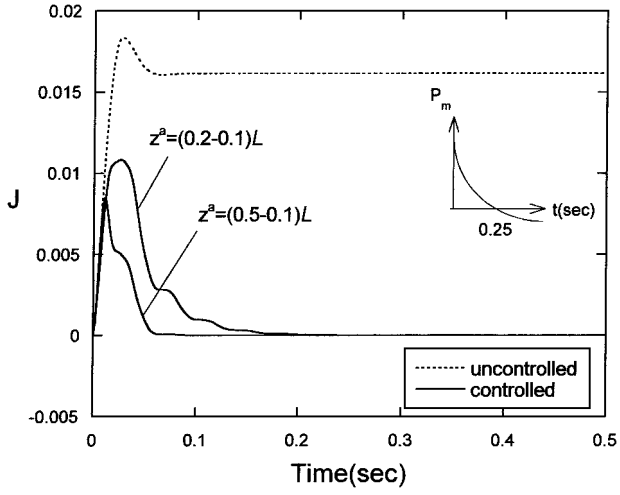

Fig. 18 Implications of the piezopatch size on total energy in the beam when subjected to a blast pulse: $a'/t_p = 80$, $t_p = 0.25$ s, $\sigma = 0.5$, $\theta = 60$ deg, and unshearable and free warping beam model.

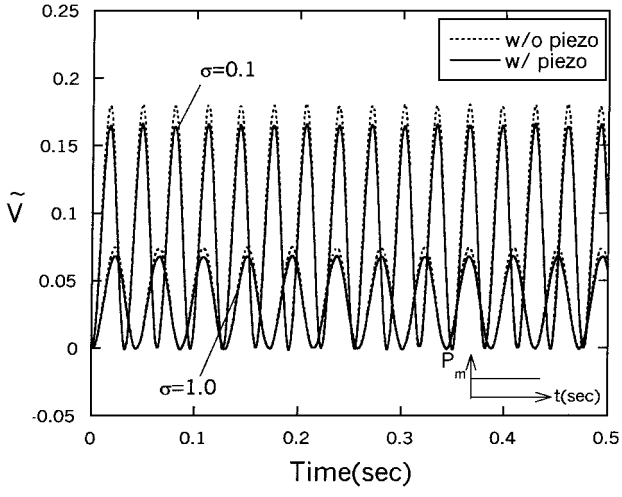

Fig. 19 Influence of including and ignoring the mass and stiffness of full span piezoactuators on the dynamic response of the beam tip to a step pulse: $\theta = 77.5$ deg, $L = 80$ in. and unshearable and free warping beam model.

be of interest. Figure 19 supplies two sets of time-history plots for the transversal deflection that correspond to the cases of the inclusion and discard of the mass and stiffness of actuators. The results correspond to two taper beam ratios, the full span piezoactuator, and to the action of a step pulse. Ignoring the mass and stiffness of the actuators results in slightly larger deflection amplitudes than the actual ones that include their effect. This effect tends, however, to decay in the case of uniform cross section beams ($\sigma = 1$) that experience larger bending stiffnesses than their tapered beam counterparts. This effect is expected further to decrease in the case of the piezopatch actuators.

Note that in the displayed results, unless otherwise stated, rotatory inertia, warping restraint, and transverse shear flexibility effects have been included. In various contexts, their implications have been discussed in Refs. 6, 9, and 10. Whereas the rotatory and warping inertia terms have a little impact on both the open- and closed-response characteristics, transverse shear effect can be rather important, especially for structures constructed of materials featuring large transverse shear flexibilities and/or high thickness ratios.

As was shown also in Ref. 6, the discard of transverse shear flexibility, implying the adoption of the classical Bernoulli–Euler hypothesis, can result in severe underestimations of the open-loop response amplitudes, but at the same time, for the closed loop response, can result in small differences as compared to those predicted within the shearable model.

Also in this context, the results not displayed here reveal that the taper ratio can play a not negligible role on the open-loop deflection time history. This consists in the increase of the differences between the classical and the shearable predictions when the taper ratio decreases and in their diminishment when it increases toward the case of the uniform cross section beams, that is, toward $\sigma = 1$.

For the closed-loop predictions, the implications of the taper ratio becomes immaterial. As concerns the warping restraint effect, the results not displayed here reveal that the implications of reducing the twist angle and deflection amplitudes in the case of the beam featuring bending–twist elastic coupling are significant, even for high aspect ratio beams, when these are built up from composite materials. In a different context, this was put into evidence, for example, in Ref. 23. However, the closed-loop response shows little difference between the predictions provided by the free and the warping restraint models.

Although, the control methodology presented here also can address the issue of the control input voltage (Refs. 5 and 6), here, with a single exception represented by the case considered in Fig. 9b, no constraint on the control input voltage was imposed.

However, in Ref. 24, a modified bang–bang control methodology enabling one to accomplish an optimal control design in the conditions of a maximum input voltage constraint was developed. Note, in this context, that the results obtained via the application of the bang–bang control shows negligible differences as compared to those obtained within the actual method, when in addition, a voltage constraint is imposed.

Finally, note that the level of the electric field and the presence of tensile stresses on the actuator, constitute factors that can significantly affect the linear variation character of the piezoelement characteristics.

A investigated in Ref. 25, these can have severe implications on the control predictions. For this reason, studies involving the validation of the theoretical findings in the light of the experimental evidence are likely to constitute a topic of extreme importance in the years to come.

Conclusions

A number of issues related with the influence of nonclassical effects on the optimal feedback control of the dynamic response of doubly tapered thin-walled beams subjected to blast pulses have been investigated. Among others, issues related to the influence of location and size of piezoelectric patches, beam aspect ratio and taper, directionality property of fibrous composite materials of the host structure, control input, and power consumption, as well as implications related to the instantaneous control methodology, have been explored. The presented results reveal the synergistic interaction and efficiency emerging from the implemented control methodology, based on the simultaneous application of the optimal feedback control and of the tailoring technique, on dynamic response of cantilevered thin-walled beams exposed to time-dependent external pressure pulses.

Appendix A: Expression of Stiffness Quantities $a_{ij}(z) = a_{ji}(z)$ and Inertia Coefficients Intervening in the Governing Equations (9) and (11)

$$a_{33}(z) = \oint \left[K_{11} y^2(z) - 2K_{14} y(z) \frac{\mathrm{d}x}{\mathrm{d}s} + K_{44} \frac{\mathrm{d}x}{\mathrm{d}s} \frac{\mathrm{d}x}{\mathrm{d}s} \right] \mathrm{d}s$$

$$a_{37}(z) = \oint \left[K_{13}(z) y(z) - K_{43}(z) \frac{\mathrm{d}x}{\mathrm{d}s} \right] \mathrm{d}s$$

$$a_{55}(z) = \oint \left[K_{22} \frac{\mathrm{d}y}{\mathrm{d}s} \frac{\mathrm{d}y}{\mathrm{d}s} + A_{44} \frac{\mathrm{d}x}{\mathrm{d}s} \frac{\mathrm{d}x}{\mathrm{d}s} \right] \mathrm{d}s$$

$$a_{56}(z) = -\oint \left[K_{21} F_\omega(s, z) \frac{\mathrm{d}y}{\mathrm{d}s} + K_{24} a(s, z) \frac{\mathrm{d}y}{\mathrm{d}s} \right] \mathrm{d}s$$

$$a_{66}(z) = \oint \left[K_{11} F_{\omega}^2(s,z) + 2K_{14} F_{\omega}(s,z) a(s,z) + K_{44} a^2(s,z)\right] \mathrm{d}s \tag{A1}$$

$$[b_1, b_4(z), b_{10}(z)] = \oint m_0 \left[1, y^2(z), F_{\omega}^2(s,z)\right] \mathrm{d}s$$

$$[b_{14}(z), b_{18}(z)] = \oint m_2 \left[\left(\frac{\mathrm{d}x}{\mathrm{d}s}\right)^2, a^2(s,z)\right] \mathrm{d}s \tag{A2}$$

In these equations,

$$K_{11} = A_{22} - \frac{A_{12}^2}{A_{11}}, \qquad K_{12} = A_{26} - \frac{A_{12}A_{16}}{A_{11}} = K_{21}$$

$$K_{13}(s,z) = K_{12}\psi(s,z), \qquad K_{14} = B_{22} - \frac{A_{12}B_{12}}{A_{11}} = K_{41}$$

$$K_{22} = A_{66} - \frac{A_{16}^2}{A_{11}}, \qquad K_{24} = B_{26} - \frac{A_{16}B_{12}}{A_{11}} = K_{42}$$

$$K_{43}(s,z) = K_{24}\psi(s,z), \qquad K_{44} = D_{22} - \frac{B_{12}^2}{A_{11}} \tag{A3}$$

denote the modified local stiffnesses.

In addition,

$$(m_0, m_2) = \sum_{k=1}^{N} \int_{h_{k=1}}^{h_{(k)}} \rho_{(k)}(1, n^2)\, \mathrm{d}n \tag{A4}$$

denote mass terms, where $\rho_{(k)}$ is the mass density of the kth layer, whereas N is the total number of layers of the structure, that is, of the host and piezoactuator layers.

A_{ij}, B_{ij}, and D_{ij} are the standard local stretching, bending–stretching, and bending stiffness quantities, respectively, and A_{44} is transverse shear stiffness.

Appendix B: The Material Properties of the Host Structure

$$E_L = 30 \times 10^6 \text{ psi}(20.68 \times 10^{10} \text{ N/m}^2)$$

$$E_T = 0.75 \times 10^6 \text{ psi}(5.17 \times 10^9 \text{ N/m}^2)$$

$$G_{LT} = 0.37 \times 10^6 \text{ psi}(2.25 \times 10^9 \text{ N/m}^2)$$

$$G_{TT} = 0.45 \times 10^6 \text{ psi}(3.10 \times 10^9 \text{ N/m}^2)$$

$$\mu_{LT} = \mu_{TT} = 0.25$$

$$\rho = 14.3 \times 10^{-5} \text{ lb} \cdot \text{s}^2/\text{in.}^4 (1528.15 \text{ kg/m}^3)$$

where subscripts L and T denote directions parallel and transverse to the fibers, respectively.

Acknowledgments

The authors express their gratitude to the anonymous reviewer for his excellent comments and suggestions that have contributed to the improvement of this paper. The paper has been funded in part by the National Research Council under the Collaboration in Basic Science and Engineering Program. The support is gratefully acknowledged by L. Librescu. The contents of this publication do not necessarily reflect the views or policies of the NRC.

References

[1]Crawley, E. F., "Intelligent Structures for Aerospace: A Technology Overview and Assessment," *AIAA Journal*, Vol. 32, No. 8, 1994, pp. 1689–1699.

[2]Chopra, I., "Review of Current Status of Smart Structures and Integrated Systems," *SPIE Smart Structures and Integrated Systems*, Society of Photo-Optical Instrumental Engineers, Bellingham, WA, Vol. 2717, 1996, pp. 20–62.

[3]Loewy, R. G., "Recent Developments in Smart Structures with Aeronautical Applications," *Journal of Smart Materials and Structures*," Vol. 5, Oct. 1997, pp. 11–42.

[4]Sunar, M., and Rao, S. S., "Recent Advances in Sensing and Control of Flexible Structures via Piezoelectric Materials Technology," *Applied Mechanics Reviews,* Vol. 52, No. 1, 1999, pp. 1–16.

[5]Na, S. S., and Librescu, L., "Oscillation Control of Cantilevers via Smart Materials Technology and Optimal Feedback Control: Actuator Location and Power Consumption Issues," *Journal of Smart Materials and Structures,* Vol. 7, No. 6, 1998, pp. 833–842.

[6]Na, S. S., and Librescu, L., "Optimal Vibration Control of Thin-Walled Anisotropic Cantilevers Exposed to Blast Loading," *Journal of Guidance, Control, and Dynamics*, Vol. 23, No. 3, 2000, pp. 491–500.

[7]Song, O., Kim, J.-B., and Librescu, L., "Synergistic Implications of Tailoring and Adaptive Materials Technology on Vibration Control of Anisotropic Thin-Walled Beams," *International Journal of Engineering Science*, Vol. 39, No. 1, 2001, pp. 71–94.

[8]Librescu, L., Meirovitch, L., and Song, O., "Vibration and Static Aeroelastic Instability of Nonuniform Thin-Walled beam Composite Wings," AIAA Paper 94-1491, April 1994.

[9]Song, O., and Librescu, L., "Free Vibration of Anisotropic Composite Thin-Walled Beams of Closed Cross-Section Contour," *Journal of Sound and Vibration*, Vol. 167, No. 1, 1993, pp. 129–147.

[10]Librescu, L., Meirovitch, L., and Song, O., "Refined Structural Modeling for Enhancing Vibrational and Aeroelastic Characteristics of Composite Aircraft Wings," *La Recherche Aerospatiale*, Vol. 1, No. 1, 1996, pp. 23–35.

[11]Bhaskar, K., and Librescu, L., "A Geometrically Non-Linear Theory for Laminated Anisotropic Thin-Walled Beams," *International Journal of Engineering Science*, Vol. 33, No. 9, 1995, pp. 1331–1344.

[12]Smith, E. C., and Chopra, I., "Formulation and Evaluation of an Analytical Model for Composite Box-Beam," *Journal of American Helicopter Society*, Vol. 36, No. 3, 1991, pp. 23–25.

[13]Jung, S. N., Nagaraj, V. T., and Chopra, I., "Assessment of Composite Rotor Blades Modeling Techniques," *Journal of the American Helicopter Society*, Vol. 44, No. 3, 1999, pp. 188–205.

[14]Rehfield, L. W., and Atilgan, A. R., "Toward Understanding the Tailoring Mechanisms for Thin-Walled Composite Tubular Beams," *Proceedings of the First USSR–US Symposium on Mechanics of Composite Materials*, edited by S. W. Tsai, J. M. Whitney, T.-W. Chou, and R. M. Jones American Society of Mechanical Engineers, Fairfield, NJ, 1989, pp. 187–196.

[15]Librescu, L., Song, O., and Rogers, C. A., "Adaptive Vibrational Behavior of Cantilevered Structures Modeled as Composite Thin-Walled Beams," *International Journal of Engineering Science*, Vol. 31, No. 5, 1993, pp. 775–792.

[16]Librescu, L., Meirovitch, L., and Song, O., "Integrated Structural Tailoring and Adaptive Materials Control for Advanced Aircraft Wings," *Journal of Aircraft*, Vol. 33, No. 1, 1996, pp. 203–213.

[17]Librescu, L., Meirovitch, L., and Na, S. S., "Control of Cantilever Vibration via Structural Tailoring and Adaptive Materials," *AIAA Journal*, Vol. 35, No. 8, 1997, pp. 1309–1315.

[18]Soong, T. T., "Active Structural Control: Theory and Practice," *Longman Scientific and Technical*, New York, 1990, pp. 75–99.

[19]Dosch, J. J., Inman, D. J., and Garcia, E., "A Self-Sensing Piezoelectric Actuator for Collocated Control," *Journal of Intelligent Material Systems and Structures*, Vol. 3, No. 2, 1992, pp. 166–184.

[20]Ha, S. K., Keilers, C., and Chang, F. K., "Finite Element Analysis of Composite Structures Containing Distributed Piezoceramic Sensors and Actuators," *AIAA Journal*, Vol. 30, No. 3, 1992, pp. 772–780.

[21]Librescu, L., and Nosier, A., "Response of Shear Deformable Elastic Laminated Composite Flat Panels to Sonic Boom and Explosive Blast Loadings," *AIAA Journal*, Vol. 28, No. 2, 1990, pp. 345–352.

[22]Park, C., Waltz, C., and Chopra, I., "Bending and Torsion Models of Beams with Induced-Strain Actuators," *Smart Materials and Structures,* Vol. 5, Feb. 1996, pp. 98–113.

[23]Librescu, L., and Khdeir, A. A., "Aeroelastic Divergence of Sweptforward Composite Wings Including Warping Restraint Effect," *AIAA Journal*, Vol. 26, No. 11, 1998, pp. 1373–1377.

[24]Na, S. S., and Librescu, L., "Modified Bang–Bang Vibration Control Strategy Applied To Adaptive Nonuniform Cantilevered Beams," *Proceedings of the 42nd AIAA/ASME/ASCE/AHS/ASC Structures, Structural Dynamics, and Material Conference and Exhibit*, Vol. 3, AIAA, Reston, VA, 2001, pp. 1888–1898.

[25]Sirohi, J., and Chopra, I., "Fundamental Behavior of Piezoceramic Sheet Actuators," *SPIE Conference on Smart Structures and Integrated Systems*, Vol. 3329, Society of Photo-Optical Instrumentation Engineers, Bellingham, WA, 1998, pp. 626–646.